Nanocrystal Grain Growth and Device Architectures for High-Efficiency CdTe Ink-Based Photovoltaics

Ryan W. Crisp,[†,‡] Matthew G. Panthani,[∥] William L. Rance,[†] Joel N. Duenow,[†] Philip A. Parilla,[†] Rebecca Callahan,[†,§] Matthew S. Dabney,[†] Joseph J. Berry,[†] Dmitri V. Talapin,[∥,*] and Joseph M. Luther[†,*]

[†]National Renewable Energy Laboratory, Golden, Colorado 80401, United States, [‡]Department of Physics, Colorado School of Mines, Golden, Colorado 80401, United States, [§]Department of Chemistry and Biochemistry, University of Colorado, Boulder, Colorado 80309, United States, and [∥]Department of Chemistry, University of Chicago, Chicago, Illinois 60637, United States

ABSTRACT We study the use of cadmium telluride (CdTe) nanocrystal colloids as a solution-processable "ink" for large-grain CdTe absorber layers in solar cells. The resulting grain structure and solar cell performance depend on the initial nanocrystal size, shape, and crystal structure. We find that inks of predominantly wurtzite tetrapod-shaped nanocrystals with arms ~5.6 nm in diameter exhibit better device performance compared to inks composed of smaller tetrapods, irregular faceted nanocrystals, or spherical zincblende nanocrystals despite the fact that the final sintered film has a zincblende crystal structure. Five different working device architectures were investigated. The indium tin oxide (ITO)/CdTe/zinc oxide structure leads to our best performing device architecture (with efficiency >11%) compared to others including two structures with a cadmium sulfide (CdS) *n*-type layer typically used in high efficiency sublimation-grown CdTe solar cells. Moreover, devices without CdS have improved response at short wavelengths.

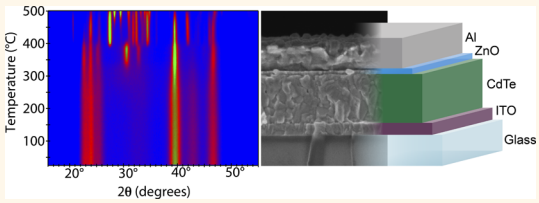

KEYWORDS: CdTe · photovoltaic · nanocrystal · grain growth · device architecture · sintering · solution-processed

Thin film photovoltaic (PV) materials offer an advantage over traditional silicon solar cells due to their larger absorption coefficients (primarily resulting from their direct band gaps), thereby reducing the total amount of material needed to absorb sunlight. Additionally, thin film materials such as CdTe, Cu(In,Ga)Se_2, $Cu_2ZnSn(S,Se)_4$, quantum dot solar cells, and perovskite materials such as $CH_3NH_3PbI_3$ can be deposited using inexpensive methods on a variety of (low cost) substrates to achieve a reduction in levelized cost of a PV system. Commercial deposition of thin-film PV absorber layers typically relies on close space sublimation or cosputtering/coevaporation to deposit compound semiconductors. Solution-processing of thin materials allows high-throughput, efficient use of precursors, and lower capital costs. However, the power conversion efficiencies of solution-based approaches in some materials currently fall behind traditional vapor deposition techniques (CdTe and Cu(In,Ga)Se_2), while other material systems' (CZTS and perovskites) solution-processed films out-perform vapor phase deposition.[1−4] The lag in record efficiency for certain absorber materials compared to vapor-phase deposition indicates a need to more fully understand and further develop solution-processed materials.

Solution-based deposition of inorganic semiconductors has been accomplished using two distinct techniques. The first general set of approaches involves chemical deposition methods. Challenges arising with chemical-deposition techniques include controlling stoichiometry, crystal grain size, phase purity, substrate limitations (e.g., needing conductive substrates for electrochemical depositions), low throughput, and effects associated with grains boundaries.[5]

A second method is the colloidal synthesis of small crystals of the material of interest (in this report 5−10 nm CdTe) that seed the growth of large grains when cast into a film and heated.[2,6−12] Colloidal synthesis prior to film deposition enables efficient use of materials yielding nearly 100% conversion of precursor into final product,[13] tunable stoichiometry,[14] and control of crystal phase.[15]

* Address correspondence to joey.luther@nrel.gov, dvtalapin@uchicago.edu.

Received for review May 5, 2014 and accepted August 18, 2014.

Published online August 18, 2014
10.1021/nn502442g

Casting solutions of NCs with spraying, dipping, blading, or spin-coating methods onto substrates forms a film, but care must be taken to prevent cracking during postdeposition treatments.[16] By using a layer-by-layer process, relatively thick (>500 nm) crack-free films can be made as sequential coatings fill in gaps in the underlying layers.[10,17] The ligands used during NC synthesis are beneficial for controlling growth kinetics, providing colloidal stability, and passivating surface states on the nanocrystal; however, they impede electronic transport and lead to insulating films.[17−19] A method of overcoming electronic transport limitations from the aliphatic insulating ligands is to remove them thermally and/or chemically. The NC solution can then be thought of as an ink for depositing a bulk film through sintering.[8−11] There is precedent for using such NC inks in PV devices. Various groups have demonstrated solar cells using this approach with CdTe NC dispersions.[9,18−21] Devices made from combinations of CdSe and CdTe NCs further demonstrate the stoichiometric control possible by using NC systems.[20,21] In another example, inks of $Cu_2ZnSn(S,Se)_4$ (CZTSSe) NCs are used in solar cells that obtain >7% power conversion efficiency (PCE). CZTS NCs are synthesized, spin-coated onto a molybdenum-coated substrate, then annealed in a Se-vapor atmosphere to expand the lattice, filling voids induced by the removal of ligands.[8] Similar approaches have been used to produce CIGSSe devices with 12% PCE.[22] However, the effects of the contacts and grain structure of ink-based cells are still not fully understood.

RESULTS AND DISCUSSION

In this work, we investigate the role of the NC ink properties (e.g., starting NC shape, crystal structure, and concentration) on grain growth as well as how device architecture and film processing further affect device performance. Through optimization of the ink and contacts, we achieved devices having power conversion efficiencies of up to 11.3%. After optimizing the ink formulation and deposition conditions to achieve high-quality thin films, we explored the viability of using the optimized ink in five different device architectures. The device structure and electrical contacts determine the energetics of the system and allow for charge extraction. In order to achieve higher efficiencies, it is important to understand how different contact materials interact with the solution-processed CdTe film.[23] In the layer-by-layer approach used here to construct CdTe absorber films, oleate-terminated NCs are dissolved in pyridine and heated to 105 °C for 24 h. This process displaces the oleate ligands, which loosely binds to Cd−chalcogenide NC surfaces and can be easily removed with mild thermal annealing.[24] Heating the NCs in pyridine also alters the stoichiometry of the nanocrystals from Cd-rich to near stoichiometric.[25] In previous reports, the CdTe NCs used were not spherical but rather rod- or tetrapod-shaped.[10,20,21,26,27] Working under the hypothesis that spherical NCs could assemble with higher packing density and therefore more easily convert into continuous films with less void space and larger grains, we synthesized different NC morphologies by modifying the reaction temperature and injection concentrations. Furthermore, the highest efficiencies in previously reported CdTe NC ink-based solar cells include an ITO/CdTe interface, whereas conventional CdTe solar cells are deposited onto CdS.[28] This suggests that CdTe ink-based cells could likely reach higher efficiencies with more conventional device structures. This work aims to test ink-based CdTe absorber films in the highly explored structures used in traditional CdTe cells.

Film Characteristics Resulting from Modification of the NC Ink. Parts A−C of Figure 1 show transmission electron microscope (TEM) images of the starting NCs synthesized by injecting tri-*n*-butylphosphine telluride (TBP-Te) into a hot cadmium oleate/octadecene mixture. By altering the injection temperature and concentration of the Te-precursor, we were able to synthesize nanocrystals with three distinct morphologies: nearly spherical (≥300 °C), faceted (<240 °C), and tetrapodal (260−275 °C) nanocrystals. This effect is not new, as Yu and co-workers also noticed similar effects by changing the Cd concentration and the ligands used during synthesis and also saw variation in crystal shape and phase; they, however, did not report the ability to synthesize tetrapods using TBP-Te.[15] Parts D and E of Figure 1 show absorbance spectra and powder X-ray diffraction (XRD) data, respectively, for the NCs before and after pyridine ligand exchange. The absorption spectra of the pyridine-capped NCs match that of the oleate-capped NCs indicating that the NC size and shape are unaffected by the pyridine treatment (dot symbols). This is supported by transmission electron microscope (TEM) images taken of the NCs before and after pyridine treatment (Figure S1, Supporting Information), which shows increased agglomeration but no change in the NC size and shape.

We also synthesized tetrapods by using tri-*n*-octylphosphine telluride (TOP-Te) and varying the TOP-Te injection concentration. Using TOP-Te vs TBP-Te allowed us to obtain three sizes of tetrapods with first exciton peaks occurring at 603, 625, and 670 nm. We first verified the result by Macdonald *et al.*[29] that larger NC size yields higher PCE devices before extending our study to examine the effects of crystal shape and phase holding the characteristic size (e.g., first exciton peak) constant. Upon spin-coating, treatment with $CdCl_2$, and brief annealing on a hot plate (as discussed in the Methods, a process referred to from here on as layer-by-layer or LbL processing), the absorption onset of all films redshift to 850 nm (Figure 1D), accompanied

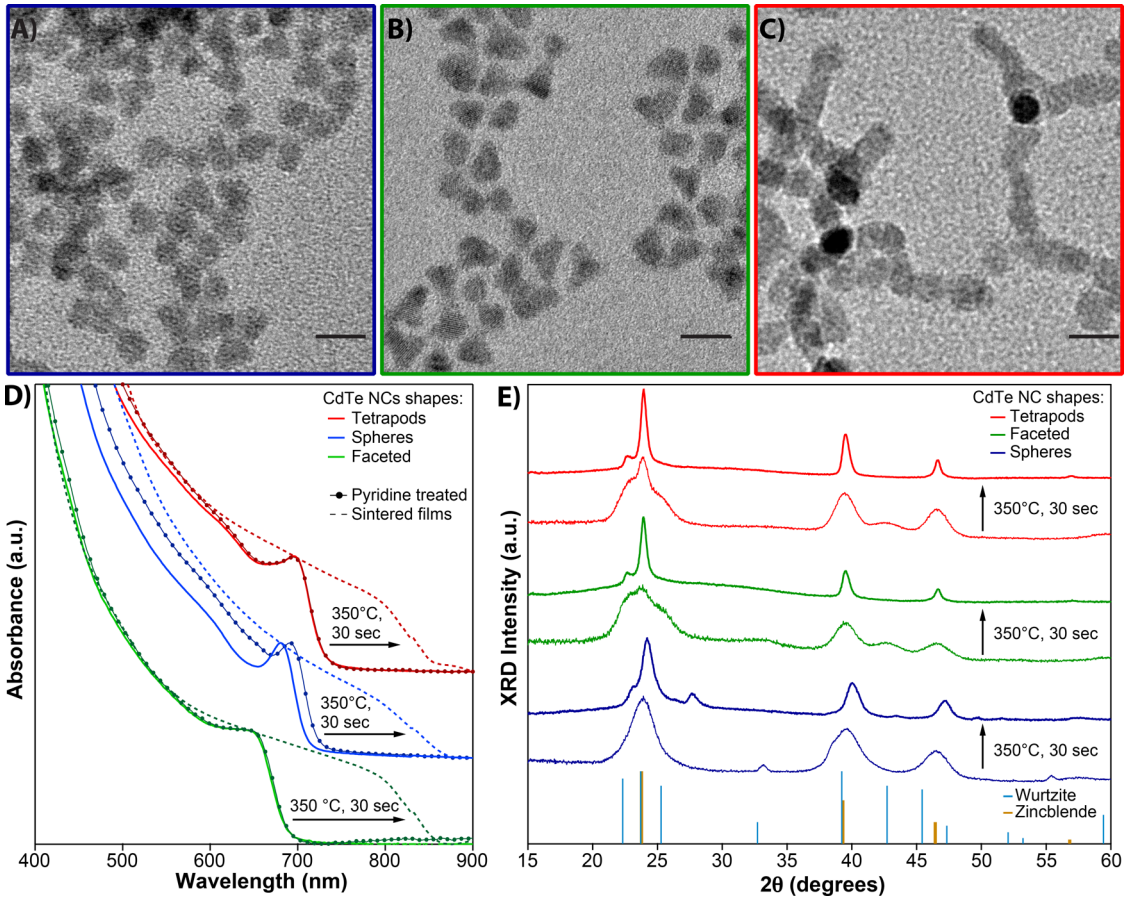

Figure 1. (A–C) TEM images of as-synthesized spheres, faceted NCs, and tetrapods, respectively, showing the uniformity of the shapes (frames are color-coded to match graph traces). (D) Absorbance spectra of the spherical (blue), faceted (green), and tetrapodal (red) NCs synthesized with oleic acid (solid lines) and after pyridine treatment (dotted lines) displaying similar absorbance spectra compared to as-synthesized NCs. Also shown are the absorbance spectra for sintered films from each of these starting NC morphologies (dashed lines). As a control, TEM images of the same samples in A–C after the pyridine treatment are shown in Figure S1 (Supporting Information), indicating that the pyridine exchange does not significantly alter the NC shape, but it is noted that the spheres slightly increased in diameter. (E) XRD data for CdTe spheres, faceted, and TPs where the faceted NCs and tetrapods show mixed wurtzite and zincblende crystal structures with the spheres showing full zincblende phase before annealing. After annealing at 350 °C for 30 s per layer (12 layers total), the films all result in the zincblende crystal structure. Standard CdTe wurtzite and zincblende patterns are shown at the bottom of (E). Peaks at 33° and 55.3° on the unannealed CdTe spheres (lower blue trace) are indicative of CdO. The peak at 22.4° in all of the annealed NC traces has been suspected to be an oxide like TeO_2 formed upon heating.[29]

by narrowing of the XRD peaks indicating the formation of large-grained CdTe. The redshift indicates a loss of quantum confinement in the sintered films. They become bulklike with the absorption onset occurring at the optical bandgap of bulk CdTe. In regard to crystal structure, the spherical NCs are zincblende whereas the tetrapods and faceted NCs are mixed phase with both zincblende and wurtzite domains. Previous studies of tetrapod-shaped NCs indicate that the core is zincblende with wurtzite arms.[30]

To further detail the temperature dependence of the sintering process, *in situ* XRD measurements were taken as a film of $CdCl_2$-treated tetrapodal NCs was heated from room temperature to 500 °C. Figure 2A shows an intensity plot of the XRD 2θ spectra as a function of temperature. The color change from blue to yellow indicates increased XRD intensity. Narrowing of the diffraction peaks as the temperature is increased over 300 °C indicates the gradual grain-growth onset. Figure 2B shows differential scanning calorimetry (DSC) data for a similar sample. In the DSC plot, an endothermic change in heat flow around 280 °C indicates loss of the remaining surface ligands but could also indicate a phase change (likely surface melting) whereas the higher temperature exothermic peak indicates recrystallization as the film converts from wurtzite to zincblende.[29] These phase changes over 300 to 400 °C correlate to the *in situ* XRD data and indicate that annealing in this temperature range indeed leads to a transition in crystallographic phase and crystallite size.

Annealing beyond 350 °C leads to the formation of $CdTeO_x$ and TeO_x as indicated by peaks in the 2θ angles between 30° and 35°. Similarly, we see a reduction in the peak intensity at 2θ = 43° (as also seen in Figure 1E, annealed red trace) as the wurtzite

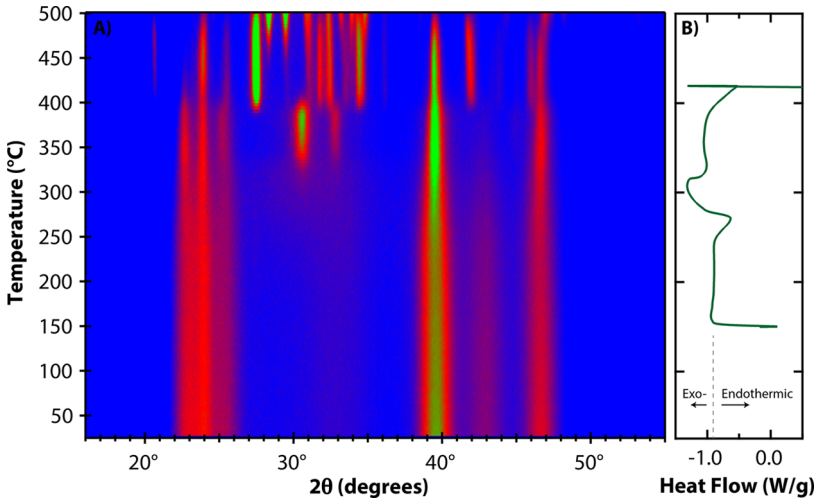

Figure 2. (A) Intensity contour plot of XRD spectra as a function of temperature. Blue color indicates low XRD intensity while yellow is high intensity. LbL processing was performed with wurtzite CdTe tetrapodal NCs, but the high-temperature annealing step was skipped. XRD measurements were taken on the sample as it was heated at 1 °C/min while the XRD signal was monitored. The temperature was varied from 25 to 500 °C. The peaks gradually sharpen as the temperature is increased, and the material converts from wurtzite to primarily zincblende. After 400 °C the film undergoes oxidation and numerous peaks appear. (B) DSC curve showing the relative heat flow as a function of temperature for wurtzite CdTe tetrapodal NCs that were drop cast and $CdCl_2$ treated. There is an endothermic peak near 280 °C that indicates that the NCs are undergoing a phase change as the surfaces begin to melt. At 320 °C there is an exothermic peak potentially indicating recrystallization into the zincblende crystal phase. The XRD and DSC data correlate well over this range where the XRD peaks sharpen and shift from wurtzite to zincblende. Note: the horizontal lines at ~150 and 410 °C in the DSC plot are artifacts of the heating and cooling process.

phase disappears above 300 °C. At temperatures beyond 400 °C, many new peaks appear and the film changed from brown to white in correlation with endothermic response shown in the DSC data. We note that this data is taken with a slow (1 °C/min) increase in substrate temperature with good thermal conductivity between the film and hot stage, whereas LbL style film progression in device fabrication involves short rapid anneals where a room temperature film is placed on a hot plate set to 350 °C for less than 1 min after each layer. Thus, the side peaks near $2\theta = 25°$ are found to not completely reduce as is found in the LbL deposition.

Film Formation and Characterization. The hot-plate temperature and duration of the thermal anneal affect device performance and film quality. As seen in Figures 1E and 2A, the rate at which the film is annealed can have an impact on proper phase conversion from wurtzite to zincblende. For high-throughput fabrication of PV modules, a rapid sintering process is desired. We found optimal performance with brief (<1 min) thermal annealing on an aluminum hot plate set to a temperature between 300 and 400 °C. This correlates to the highest temperature for pure CdTe phases before the onset of oxide formation above 350 °C. We find that annealing at 350 °C for 30 s leads to the largest grains and highest efficiency. After LbL processing, all films have a zincblende crystal structure. Without $CdCl_2$ treatment or if the $CdCl_2$ is rinsed off before sintering, the NCs do not sinter into large grains (Figure S2, Supporting Information), and devices fabricated in this manner perform poorly due to low J_{sc}. When the $CdCl_2$ treatment is optimized, the CdTe films become dense (Figure S2, Supporting Information), convert to zincblende phase, and grow into larger grains as Figure S1 (B, D, F) (Supporting Information) shows with cross-sectional SEM images of films sintered from the different shapes of pyridine-treated NCs. Use of tetrapod-shaped NCs leads to smooth films with the largest grain size and least amount of void space. The films possess columnar grains that extend throughout the entire active layer even though the sintering process is occurring a layer at a time. The lack of visible individual layers in the SEM images indicates that each subsequent layer recrystallizes into the previous layers to form continuous grains. We find that grains appear larger and pore sizes are smaller with higher temperature/shorter annealing processes, while the absorbance spectra are very similar in all cases tested (Figure S3 and Figure S4, Supporting Information). The larger grains and reduced pore sizes likely promote charge carrier transport. Panthani *et al.*[27] attributed the increase in efficiency over similar solar cells reported by Jasieniak *et al.*[10] to larger grains extending throughout the active layer. Here we have determined what factors lead to the optimal grain growth by varying the starting ink composition and the device architecture. Investigating the factors influencing grain-growth explains how each layer amalgamates into the previous ones as the NCs undergo a phase transition from wurtzite to zincblende.

Effects of the Device Structure on Performance of CdTe Ink-Based Solar Cells. We investigated multiple device architectures in both substrate and superstrate configurations

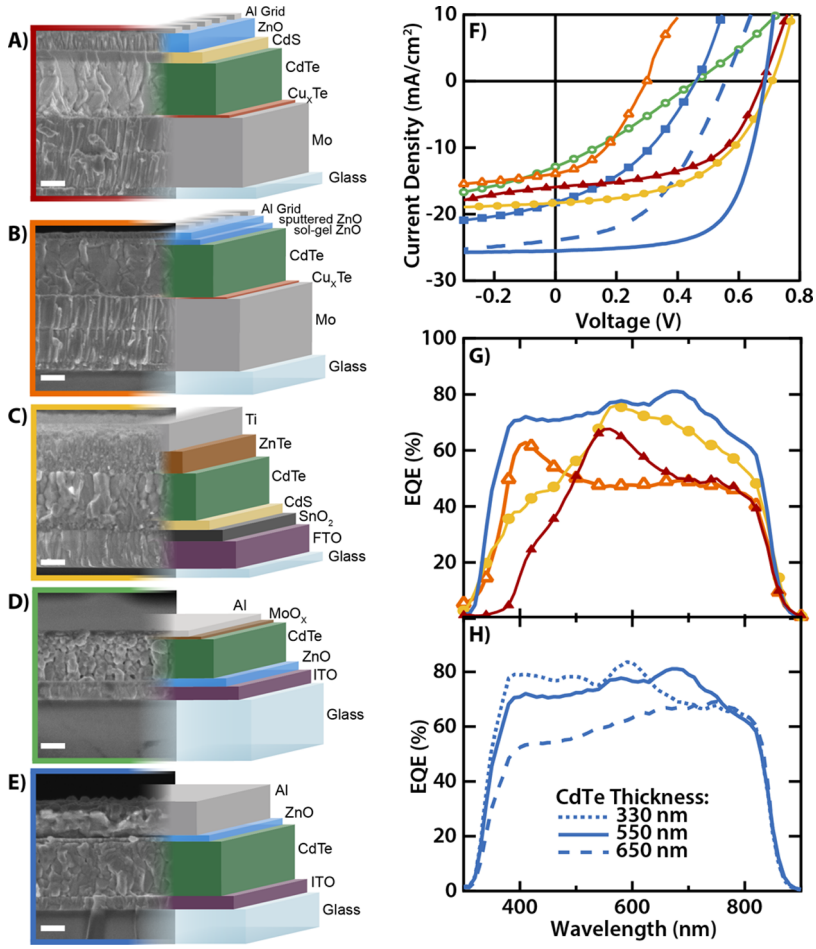

Figure 3. SEM cross-sections and schematic representations of device architectures used in this study. Structures in panels A and B are substrate configurations where the light is incident on the top of the device stack. Structures in panels C–E are superstrate configurations where the light is incident upon the glass before being absorbed in the CdTe layer. The bottom SEM shows the *n*-type layer made with ZnO:In (1%) *via* sol–gel but ZnO deposition methods using NC–ZnO and pulsed laser deposition were also constructed as discussed. In each cell, either the ZnO or the CdS side of the heterojunction is the anode. Scale bars are 250 nm. (F) Current–voltage characteristics from devices made from each of the structures, each employing a CdTe film spin-coated from NCs on the order of 550 nm thick. (G) External quantum efficiency (EQE) of four of the most promising structures. (H) shows EQE for three thicknesses: 330 nm (dotted line), 550 nm (solid line), and 650 nm (dashed line) of CdTe employed in the structure shown in (E) with all three thicknesses having PCE ≥10%. The legend for the symbols in panels F and G is given in Table 1, and the frame color of panels A–E corresponds to the trace colors in panels F–H.

with various contact materials to the CdTe layer. Figure 3 shows schematic layouts for various device structures along with cross-sectional SEM images of completed devices with their performance characteristics. Optimized devices utilize a ~550 nm thick CdTe absorber fabricated *via* spin coating a CdTe ink composed of tetrapods with a concentration of 40 mg/mL with each layer annealed at 350 °C for 30 s (see Figure S5, Supporting Information). Panthani *et al.* recently reported that subjecting the devices to a forward bias current soak under illumination improves the interfacial energetics at the *p*-CdTe/*n*-ITO interface yielding power conversion efficiencies >12%.[27] We find that the choice of substrate affects the CdTe grain size and morphology. Molybdenum-coated glass substrates with a 5 nm Cu_xTe layer lead to the largest grains (300 nm on average) with minimal void space (<1 pore/μm^2) observed in the CdTe layer as measured from the SEM cross sections given in Figure 3A–E. Depositing the CdTe layer on top of sol–gel ZnO leads to the smallest grains and most voids in the CdTe film (Figure 3A–E). Figure 3F shows current–voltage (JV) characteristics under AM1.5 illumination for each of the device types with device parameters shown in Table 1. To briefly describe the device structures, two devices (Figure 3A,B) were fabricated in a substrate configuration where light is incident through the top of the device stack rather than through the glass. For these cells, a transparent conducting oxide (TCO) layer was used as the top electrode along with an Al grid to reduce the devices' series resistance. CdS or ZnO:In (1%) act as window layers for these structures (parts A and B, respectively, of Figure 3). Some benefits of using a substrate design are removal of the absorption and reflection of a glass superstrate, as well as separating the CdTe growth from the junction formation. Drawbacks of the substrate structures include the inability to apply various treatments to

TABLE 1. Performance Characteristics of Each Device Structure

Structure	V_{oc} (mV)	J_{sc} (mA/cm^2)	*FF* (%)	PCE (%)
A	679	15.9	54.9	5.94
B	299	13.9	39.8	1.66
C	709	18.3	51.3	6.66
D	460	12.9	28.8	1.73
E:NC-ZnO	459	18.3	38	3.19
E:PLD	556	23.9	44.9	6.00
E:sol-gel	686	25.5	64.7	11.3

the CdTe to improve the ohmic behavior of the back contact. We also use a traditional CdTe architecture (Figure 3C)—a superstrate design in which light is incident through the glass substrate and then passes through a TCO and CdS window layer. Superstrate devices Figure 3D,E each employ ZnO rather than CdS as the *n*-type component of the heterostructure with light incident through the glass in each case; however, these devices have opposite polarity controlled by the contact layers. The benefits to using a superstrate structure include exposing the back of the CdTe to chemical and physical treatments that allow for improved contact (like the addition of copper at that interface). Limitations to this structure include increased reflection and absorption from the glass and the formation of a $CdTe_xS_{1-x}$ alloy.[31] Finally, the device structure in Figure 3E was further expanded by depositing the ZnO layer *via* three different routes: sol–gel, nanocrystalline ZnO (NC–ZnO), and pulsed laser deposition (PLD) (all described in detail in the Methods).

We found that the highest EQE across the largest spectral width is obtained using a superstrate configuration with a sol–gel ZnO:In heterojunction (Figure 3G). ZnO is transparent to light with a wavelength greater than ~375 nm, whereas CdS absorbs photons with wavelength shorter than 515 nm, allowing for increased collection of higher energy photons. This difference in photon collection accounts for the reduced EQE in the blue spectral region for devices employing a CdS window layer (Figure 3A ,C). By using a thin absorber layer in the inverted superstrate structure (Figure 3E) longer wavelength photons likely make two passes through the absorber layer due to reflection off the Al contact. The increased optical path length due to reflection gives an effective thickness greater than the ~550 nm physical thickness, allowing more long-wavelength light to be absorbed. Furthermore, using a very thin CdTe layer allows for efficient collection of blue light even though the charge-separating junction is located at the rear of the cell rather than the incident side. However, the depletion region (calculated by Panthani *et al.* for a similar device to be ~400 nm[27]) extends throughout most of the CdTe layer, thus allowing collection of the blue light absorbed in the first tens of nanometers. In an effort to increase the spectral response in the 300–550 nm spectral range of devices using CdS (structures in Figure 3A,C), the CdS layer was replaced with ZnO:In (1%) *via* the sol–gel route. Comparing the structure shown in Figure 3A to the one in Figure 3B shows that, indeed, replacing the CdS with ZnO leads to a greater blue response (from ~25% to over 60% EQE). Unfortunately, the devices shown in Figure 3B had significantly lower collection efficiency in the 600–700 nm spectral region. As a result, the overall photocurrent suffered by 2 mA/cm^2 (see Table 1). Comparing the structure shown in Figure 3C to the one in Figure 3E, there is greater spectral response in the blue region, indicating that using ZnO allows for better collection of the higher energy photons.

We fabricated a device using the standard superstrate configuration (Figure 3C). In this device, the CdS layer is thinner compared to the substrate device shown in Figure 3A (80 nm vs 115 nm) so the blue losses are not as severe, resulting in a larger J_{SC} of 18.3 mA/cm^2. Utilizing an ITO anode and ZnO:In *n*-type layer in devices leads to a synergistic effect that allows for large photocurrent (~25 mA/cm^2, see Table 1) and an appreciable V_{oc} > 680 mV after a short light soak in forward bias as described previously and in the Methods.[27] Other reports have noted transient light soaking behavior drastically increasing the PCE due to trap filling in solution-processed metal oxide layers.[32,33] We further investigated modulating the In concentration in the ZnO sol–gel (details in the Methods). Indium doping can increase the crystallinity of ZnO sol–gel films, increasing the electronic mobility by reducing grain boundary scattering.[34] Kim *et al.* found that 3% doping leads to an increase in crystallinity and a reduction in the texture coefficient of sol–gel deposited films.[34] Figure S6 (Supporting Information) shows the device performance for devices using ZnO:In layers doped with a 0, 1, 3, and 10% atomic ratio of In to Zn. 1% In doping gave the best efficiency, although the highest V_{oc} is obtained with slightly more In. From this structure, we further optimized the CdTe deposition conditions, as discussed above, and achieved device efficiencies nearing 12%. Attempts to use ZnO–NCs in these devices leads to reduced FF and V_{oc} compared to the sol–gel ZnO. The reduction in FF has been attributed to the increased series resistance in the ZnO films composed of NCs in previous reports.[27]

In addition to solution-processed ZnO deposited from NC solutions and sol–gel methods as discussed above and in ref 27, PLD ZnO was tested to determine if ZnO is the limiting layer. Using PLD, the electronic properties of ZnO can be modulated by changing the partial pressure of O_2 during deposition. This affects the position of the Fermi level as well as the conductivity. Furthermore, by changing the deposition conditions during growth, the energy band profile within the ZnO layer can be adjusted. In an effort to increase carrier extraction, a bilayer structure was explored that

introduced a highly conductive PLD ZnO layer directly on the CdTe as well as a lower conductivity PLD ZnO capping layer above the conductive layer to aid in reducing interfacial carrier recombination. We found that the bilayer structure improved performance, leading to high J_{sc} but lower power conversion efficiency than devices using sol–gel ZnO. Devices with ZnO–NCs had higher series resistance (12.25 Ω cm^2) than those with PLD ZnO (9.08 Ω cm^2) and sol–gel ZnO (3.19 Ω cm^2), which trends with device performance indicating that not only crystallinity but dopant levels play a significant role in device performance.

The superstrate device structure with a ZnO *n*-type layer (Figure 3D) aims to solve the potential problem of having the junction at the back of the optical path by positioning the *n*-type ZnO layer at the light incidence side but suffers from large series resistance and poor FF shown in the JV curves of Figure 3F and Table 1. The decreased performance could potentially be due to degradation of the ZnO during the CdTe processing steps. We also observe greater void space and a smaller CdTe grain size when depositing on ZnO compared to depositing on ITO (<100 nm average grain dimension *vs* ~200 nm, respectively. Pore sizes range from 25 to 9 nm and pore areal density changes from ~46 to ~2.5 pore/μm^2 when grown on ZnO *vs* ITO, respectively). This likely impedes charge transport within the CdTe film as an increased number of grain boundaries could lead to increased grain-boundary scattering, leading to the reduction in mobility and thus device performance. The series resistance for the device in Figure 3D was 30.9 Ω cm^2 compared to 8.5 Ω cm^2 for both structures in Figure 3A,C, indicating that increased series resistance plays a role in device performance.

Using a structure utilizing a sol–gel ZnO layer, we varied the thickness of the CdTe film to explore the effect of absorber thickness on photocurrent generation and achieved >10% efficiency for CdTe film thicknesses between 330 and 650 nm. As shown in Figure 3H, greater blue response is observed for the thinnest device, as the higher energy photons are absorbed closer to the CdTe/ZnO junction and in the depletion region. However, using thinner absorber layers results in lower EQE at longer wavelengths due to reduced absorption of low energy photons. The EQE of the thickest device monotonically decreases with decreasing wavelength because photogenerated charges further away from the junction (in the first few nanometers of the device) have lower probability for collection due to short carrier diffusion lengths. Optimized devices have thicknesses around 550 nm where the sum of losses from these mechanisms is minimized.

It is surprising that we do not observe our highest power conversion efficiency using structures like in Figure 3A,C that have demonstrated PCE >15% and >13%, respectively, with CSS-CdTe.[28,35] We find that ZnO:In sol–gel approach on ITO yields the most appropriate structure for CdTe films made from NCs. On the basis of the broad spectral response, larger open-circuit voltage, and best FF, the device structure in Figure 3E shows the most promise for efficiently extracting photogenerated charges from smooth and thin CdTe films made of sintered NCs.

CONCLUSIONS

This study explores grain growth of sintered CdTe NC-based absorber layers and device performance in various device architectures. We examined various NC shapes: spheres, faceted NCs, and tetrapods. We found that larger tetrapods spin-coated in a layer-by-layer process at lower concentration in solution form the largest grains and produce the highest efficiency devices. By utilizing the well-studied vacuum processed CdTe structures and comparing them to the structures used in most CdTe NC ink device reports,[10,20,21,26,27] we show that CdTe deposited from NC inks behaves differently in various structures and that an ITO contact with a CdTe/ZnO heterojunction in conjunction with solution processing results in the highest efficiency devices. We find that such solution-processed CdTe and ZnO films yield high efficiency devices that enable broader-band spectral response compared to CdS as is traditionally used in CdTe PVs. Respectable efficiencies are achievable using this ink-based approach that allow for a thin, smooth, CdTe absorber layer deposited without high-temperature or high-vacuum processing. The ZnO layer that yields highest power conversion efficiency is processed using a sol–gel approach with 1% doping with indium. This device structure yields comparable photocurrent density to the highest performance CdTe devices but has a V_{oc} that is ~200 mV lower. This report serves as a first step in fully understanding the grain growth required for utilizing NC-based inks in commercial PV modules. This work also demonstrates that solution-processed absorber layers for other material systems may require changes in solar cell device structure from those of vapor-phase deposition.

METHODS

Nanocrystal Synthesis. All chemicals and powders were purchased from Sigma-Aldrich and used as received. CdTe NCs were synthesized by slight modification of the synthesis described by Jasieniak *et al.*[10] and Panthani *et al.*[27] For the tetrapod synthesis, in brief, 1.25 g of CdO and 11.4 g of oleic acid (OA) were dispersed in 150 mL of octadecene (ODE) and stirred in a three-neck flask and degassed at 100 °C under vacuum for 20 min. The flask was filled with nitrogen, and the solution temperature was increased to 270 °C at which point the solution turned clear. Nine milliliters of 0.75 M solution of

tri-*n*-butylphosphine telluride (TBP-Te) mixed with 10 mL of ODE was injected at 270 °C, and the flask was immediately taken off the heating mantle and cooled naturally to room temperature. For the faceted NC synthesis, 0.26 g of CdO and 4.4 g of OA were dispersed in 60 mL of ODE, stirred in a three-neck flask, and degassed at 100 °C under vacuum for 20 min. The flask was filled with nitrogen and the solution heated to 260 °C until the solution turned clear. It was then cooled to 235 °C, and once the temperature was stable, 2 mL of 0.75 M solution of TBP-Te mixed with 4 mL of ODE was injected and the flask immediately taken off the heating mantle and cooled naturally to room temperature. For the sphere-shaped NC synthesis, 74 mg of CdO and 0.6 mL of OA were dispersed in 30 mL of ODE, stirred in a three-neck flask, and degassed at 100 °C under vacuum for 20 min. The solution was heated to 310 °C where it first turned clear and then slightly gray (following the procedure outlined by Kloper *et al.*[36]), at which point 0.95 mL of 0.75 M TBP-Te mixed with 5 mL of ODE were injected and the reaction was immediately taken off the heating mantle and allowed to cool naturally. For all CdTe syntheses, the nanocrystals were precipitated with ethanol and redispersed in hexane in air. This process was repeated three times to remove excess ligands and unreacted precursors. The purified nanocrystals were then moved into a glovebox and redispersed in hexane where they were kept until the pyridine treatment was performed. A portion of the NCs were precipitated with ethanol and redispersed in pyridine at a concentration of ~20 mg/mL. The CdTe NCs in pyridine were stirred in the glovebox overnight on a hot plate set to 105 °C. This solution was precipitated with hexane and redispersed in a 1:2 vol/vol mixture of pyridine and 1-propanol at a concentration of 40 mg/mL and stored in the glovebox until needed.

CdTe Film Processing. CdTe nanocrystals were deposited on the various substrates (first cleaned by sonicating in acetone and then 2-propanol for 5 min each) by spin-coating at 1000 rpm for 60 s. When solution is added onto the substrate before spinning, it is important to cover the entire substrate because irregularities in the film thickness and smoothness can develop and propagate across the substrate as a result of bare spots. The substrates were placed onto a hot plate held at 150 °C for 2 min followed by a dip in a saturated solution of $CdCl_2$ dissolved in methanol at 58 °C (~400 mg $CdCl_2$ in 35 mL MeOH). When not in use, the $CdCl_2$ solution was stirred at this temperature, but when the substrates were dipped into it, the stirring was stopped. On some occasions the vigorous stirring caused the CdTe to flake off the substrate and also caused visible $CdCl_2$ buildup on the film. The substrates were swiftly removed from the $CdCl_2$ solution, dipped into 2-propanol, then rinsed with 2-propanol and dried with a stream of dry air. The substrate was then placed on a second hot plate held at various temperatures, as measured by a thermocouple, but typically 350 °C for 30 s then swiftly removed and placed on a room temperature Al block. This process was repeated multiple times (typically 12−14) to build a film of the desired thickness.

Contact Layer Processing and Device Completion. In-doped CdS for device structures in Figure 3A,B was deposited by radio frequency magnetron sputtering at room temperature from a target with a composition of 0.5 mol % In_2S_3 in CdS. The film was grown to a thickness of 115 nm in an ambient of 2 vol % O_2 in Ar at a power of 60 W. The device structure in Figure 3C was fabricated as described by Rose *et al.*[37] and Gessert *et al.*[38] aside from the deposition and processing of the CdTe layer. The CdTe solar cells in device in Figure 3C were mesa-isolated with an area of 0.25 cm^2, while the cells in the device in Figure 3A ,B were isolated by scribing and had a nominal area of 0.42 cm^2. Figure S7 (Supporting Information) shows the additional processing steps used to optimize devices in Figure 3A,C. By applying a postcontact anneal of 250 °C for 5 min for the device in Figure 3A and varying the deposition temperature of the ZnTe:Cu for device in Figure 3C from 310 °C to room temperature and then applying a short postcontact anneal, we found an improvement in the V_{oc}, J_{sc}, and FF for these devices. The device in Figure 3B saw no such improvement with further annealing.

ZnO NCs were synthesized by adding 0.44 g of Zn acetate dihydrate to 40 mL of ethanol in a flask and heating at 60 °C. After 30 min of heating, 2 mL of tetramethylammonium hydroxide (20% in MeOH) in 10 mL of ethanol was added dropwise to the solution over 5 min similarly to Wood *et al.*[39] The ZnO nanoparticle solution was heated at 60 °C for 30 min to attain the ZnO NCs of 5 nm in size. ZnO NCs dispersed in their growth solution were precipitated with hexane and centrifuged. The supernatant was discarded, and the precipitated nanoparticles were redispersed in 1-propanol at a concentration of 40 mg/mL. The ZnO NCs were then spin-coated at 900 rpm for 60 s prior to a 2 min heat treatment on a hot plate set to 300 °C to dry residual solvent.

One variation of the device in Figure 3E employs ZnO as deposited by pulsed laser deposition as discussed in ref.[40] The PLD system had a base pressure of $<1.0 \times 10^{-6}$ Torr and ablates material with a KrF laser operating at 248 nm. For these experiments, a pulse energy of 280 mJ at 5 Hz repetition rate was used to deliver an energy density to the target of approximately 0.76 J/cm^2 after optical losses. Depositions of 80−100 nm of material typically took 1 h. The substrate temperature and chamber atmosphere were fixed at 300 °C and 1.1×10^{-3} Torr partial pressure of oxygen, respectively, for the first half of the deposition then the heater was turned off and the sample cooled naturally before the last 50 nm were deposited. The substrate was mounted to the heater block using silver paint to increase thermal conductivity.

ZnO:In sol gel was prepared in a similar manner as Ohyama *et al.*[41] and similar to our previously published work[42] by dissolving 1.2 g Zn acetate dihydrate in 12 mL of 2-methoxyethanol and 0.31 mL of ethanolamine. Indium was introduced by addition of various atomic percentages as described in the manuscript from direct addition of $InCl_3$ into the sol−gel mixture. This solution was then spin-coated onto a substrate at 3000 rpm followed by annealing at 300 °C (measured by a thermocouple) on a hot plate in air for 2 min. The physical characteristics of the ZnO films from all three deposition methods can be found in the associated references.

MoO_x and Al top contacts were thermally evaporated following the procedure described by Gao *et al.*[23] The MoOx was needed in the structure shown in Figure 3D to provide a p-type contact to the CdTe layer similar to the work done by Lin *et al.*[43,44] The structures in Figure 3D,E used circular top contacts evaporated through a shadow mask on unpatterned ITO with a nominal area of 0.11 cm^2.

Device Characterization and Testing. Sample annealing was monitored with *in situ* X-ray diffraction (XRD) using a Bruker D8 Discover with a Vantec area detector (sample-to-detector distance of 15 cm) and an Anton Paar DHS 900 hot stage. The sample was placed on the hot stage with spring clips and illuminated with X-rays from a copper target (40 kV, 35 mA) using a Göebel mirror (parallel optics) and 1 mm circular collimator. The stage was ramped to 500 °C from room temperature in air at a 1 °C/min ramp rate, and 3 min XRD data frames centered at ~36° 2θ were acquired every ~3.5 min starting with the temperature ramp onset. The nominal temperature for each data frame is the average temperature during that data frame.

Completed solar cells were tested on a Newport class B solar simulator. The light intensity was adjusted to match the current output of a reference GaAs solar cell to the predetermined AM1.5 photoresponse as measured by the measurements and characterization group at NREL. The light soak under forward bias (Current/light soak) was done by holding the cell under +3 V forward bias and monitoring the current as it slowly increases under 1-sun illumination. After roughly 10 min, the current plateaus at ~0.2 A, then the V_{oc} is monitored and slowly increases as well; once it also stabilizes, the JV scan is run from +1 to −0.4 V. Only devices with a CdTe/ITO interface show an increase in efficiency with current/light soaking as shown in Figure S8 (Supporting Information). In order to verify the stability of the devices after current/light soaking, the JV scan was run repeatedly in both directions (forward to reverse bias and reverse to forward bias) and found to remain steady after a small initial drop as shown Figure S9 (Supporting Information). Similar effects have been found in other systems with other metal oxide *n*-type layers.[32,33]

Conflict of Interest: The authors declare no competing financial interest.

Acknowledgment. This work is supported by the U.S. Department of Energy (DOE) SunShot program under Award No. DE-EE0005312. Support for the vapor-deposited or sputtered contact materials from the Center for Interface Science: Solar Electric Materials (CISSEM), an Energy Frontier Research Center funded by the US Department of Energy, Office of Science, Office of Basic Energy Sciences, under Award Number DE-SC0001084 and the U.S. Department of Energy under Contract No. DE-AC36-08-GO28308 with the National Renewable Energy Laboratory, is acknowledged. We thank B. To for SEM imaging and R.T. Collins and M.O. Reese for helpful discussions.

Supporting Information Available: TEM and SEM images characterizing the NC ink, extensive data on device optimization, and current/light soaking effects. This material is available free of charge *via* the Internet at http://pubs.acs.org.

REFERENCES AND NOTES

1. Todorov, T. K.; Tang, J.; Bag, S.; Gunawan, O.; Gokmen, T.; Zhu, Y.; Mitzi, D. B. Beyond 11% Efficiency: Characteristics of State-of-the-Art Cu2znsn(S,Se)(4) Solar Cells. *Adv. Energy Mater.* **2013**, *3*, 34–38.
2. Akhavan, V. A.; Goodfellow, B. W.; Panthani, M. G.; Steinhagen, C.; Harvey, T. B.; Stolle, C. J.; Korgel, B. A. Colloidal Cigs and Czts Nanocrystals: A Precursor Route to Printed Photovoltaics. *J. Solid State Chem.* **2012**, *189*, 2–12.
3. Stolle, C. J.; Harvey, T. B.; Korgel, B. A. Nanocrystal Photovoltaics: A Review of Recent Progress. *Curr. Opin. Chem. Eng.* **2013**, *2*, 160–167.
4. He, M.; Zheng, D.; Wang, M.; Lin, C.; Lin, Z. High Efficiency Perovskite Solar Cells: From Complex Nanostructure to Planar Heterojunction. *J. Mater. Chem. A* **2014**, *2*, 5994–6003.
5. Mitzi, D. B. Solution Processing of Chalcogenide Semiconductors *via* Dimensional Reduction. *Adv. Mater.* **2009**, *21*, 3141–3158.
6. Akhavan, V. A.; Harvey, T. B.; Stolle, C. J.; Ostrowski, D. P.; Glaz, M. S.; Goodfellow, B. W.; Panthani, M. G.; Reid, D. K.; Vanden Bout, D. A.; Korgel, B. A. Influence of Composition on the Performance of Sintered Cu(in,Ga)Se2 Nanocrystal Thin-Film Photovoltaic Devices. *ChemSusChem* **2013**, *6*, 481–486.
7. Ford, G. M.; Guo, Q.; Agrawal, R.; Hillhouse, H. W. Cuin(S, Se)(2)Thin Film Solar Cells from Nanocrystal Inks: Effect of Nanocrystal Precursors. *Thin Solid Films* **2011**, *520*, 523–528.
8. Guo, Q.; Ford, G. M.; Yang, W.-C.; Walker, B. C.; Stach, E. A.; Hillhouse, H. W.; Agrawal, R. Fabrication of 7.2% Efficient Cztsse Solar Cells Using Czts Nanocrystals. *J. Am. Chem. Soc.* **2010**, *132*, 17384–17386.
9. Guo, Q.; Hillhouse, H. W.; Agrawal, R. Synthesis of Cu2znsns4 Nanocrystal Ink and Its Use for Solar Cells. *J. Am. Chem. Soc.* **2009**, *131*, 11672.
10. Jasieniak, J.; MacDonald, B. I.; Watkins, S. E.; Mulvaney, P. Solution-Processed Sintered Nanocrystal Solar Cells *via* Layer-by-Layer Assembly. *Nano Lett.* **2011**, *11*, 2856–2864.
11. Puthussery, J.; Seefeld, S.; Berry, N.; Gibbs, M.; Law, M. Colloidal Iron Pyrite (Fes2) Nanocrystal Inks for Thin-Film Photovoltaics. *J. Am. Chem. Soc.* **2011**, *133*, 716–719.
12. Pehnt, M.; Schulz, D. L.; Curtis, C. J.; Jones, K. M.; Ginley, D. S. Nanoparticle Precursor Route to Low-Temperature Spray Deposition of Cdte Thin Films. *Appl. Phys. Lett.* **1995**, *67*, 2176–2178.
13. Li, L.; Pandey, A.; Werder, D. J.; Khanal, B. P.; Pietryga, J. M.; Klimov, V. I. Efficient Synthesis of Highly Luminescent Copper Indium Sulfide-Based Core/Shell Nanocrystals with Surprisingly Long-Lived Emission. *J. Am. Chem. Soc.* **2011**, *133*, 1176–1179.
14. Luther, J. M.; Pietryga, J. M. Stoichiometry Control in Quantum Dots: A Viable Analog to Impurity Doping of Bulk Materials. *ACS Nano* **2013**, *7*, 1845–1849.
15. Yu, W. W.; Wang, Y. A.; Peng, X. Formation and Stability of Size-, Shape-, and Structure-Controlled Cdte Nanocrystals: Ligand Effects on Monomers and Nanocrystals. *Chem. Mater.* **2003**, *15*, 4300–4308.
16. Law, M.; Luther, J. M.; Song, Q.; Hughes, B. K.; Perkins, C. L.; Nozik, A. J. Structural, Optical, and Electrical Properties of Pbse Nanocrystal Solids Treated Thermally or with Simple Amines. *J. Am. Chem. Soc.* **2008**, *130*, 5974–5985.
17. Luther, J. M.; Law, M.; Song, Q.; Perkins, C. L.; Beard, M. C.; Nozik, A. J. Structural, Optical and Electrical Properties of Self-Assembled Films of Pbse Nanocrystals Treated with 1,2-Ethanedithiol. *ACS Nano* **2008**, *2*, 271–280.
18. Law, M.; Luther, J. M.; Song, O.; Hughes, B. K.; Perkins, C. L.; Nozik, A. J. Structural, Optical, and Electrical Properties of Pbse Nanocrystal Solids Treated Thermally or with Simple Amines. *J. Am. Chem. Soc.* **2008**, *130*, 5974–5985.
19. Talapin, D. V.; Murray, C. B. Pbse Nanocrystal Solids for N- and P-Channel Thin Film Field-Effect Transistors. *Science* **2005**, *310*, 86–89.
20. Gur, I.; Fromer, N. A.; Geier, M. L.; Alivisatos, A. P. Air-Stable All-Inorganic Nanocrystal Solar Cells Processed from Solution. *Science* **2005**, *310*, 462–465.
21. MacDonald, B. I.; Martucci, A.; Rubanov, S.; Watkins, S. E.; Mulvaney, P.; Jasieniak, J. J. Layer-by-Layer Assembly of Sintered Cdsexte1-X Nanocrystal Solar Cells. *ACS Nano* **2012**, *6*, 5995–6004.
22. Guo, Q.; Ford, G. M.; Agrawal, R.; Hillhouse, H. W. Ink Formulation and Low-Temperature Incorporation of Sodium to Yield 12% Efficient Cu(in,Ga)(S,Se)2 Solar Cells from Sulfide Nanocrystal Inks. *Prog. Photovoltaics* **2013**, *21*, 64–71.
23. Gao, J.; Perkins, C. L.; Luther, J. M.; Hanna, M. C.; Chen, H.-Y.; Semonin, O. E.; Nozik, A. J.; Ellingson, R. J.; Beard, M. C. N-Type Transition Metal Oxide as a Hole Extraction Layer in Pbs Quantum Dot Solar Cells. *Nano Lett.* **2011**, *11*, 3263–3266.
24. Ridley, B. A.; Nivi, B.; Jacobson, J. M. All-Inorganic Field Effect Transistors Fabricated by Printing. *Science* **1999**, *286*, 746–749.
25. Anderson, N. C.; Hendricks, M. P.; Choi, J. J.; Owen, J. S., Ligand Exchange and the Stoichiometry of Metal Chalcogenide Nanocrystals: Spectroscopic Observation of Facile Metal-Carboxylate Displacement and Binding. *J. Am. Chem. Soc. 135*, 18536−18548.
26. Olson, J. D.; Rodriguez, Y. W.; Yang, L. D.; Alers, G. B.; Carter, S. A. Cdte Schottky Diodes from Colloidal Nanocrystals. *Appl. Phys. Lett.* **2010**, *96*, 242103.
27. Panthani, M. G.; Kurley, J. M.; Crisp, R. W.; Dietz, T. C.; Ezzyat, T.; Luther, J. M.; Talapin, D. V., High Efficiency Solution Processed Sintered Cdte Nanocrystal Solar Cells: The Role of Interfaces. *Nano Lett. 14*, 670−675.
28. Britt, J.; Ferekides, C. Thin-Film Cds/Cdte Solar-Cell with 15.8-Percent Efficiency. *Appl. Phys. Lett.* **1993**, *62*, 2851–2852.
29. MacDonald, B. I.; Gengenbach, T. R.; Watkins, S. E.; Mulvaney, P.; Jasieniak, J. J. Solution-Processing of Ultra-Thin Cdte/Zno Nanocrystal Solar Cells. *Thin Solid Films* **2014**, *558*, 365–373.
30. Talapin, D. V.; Nelson, J. H.; Shevchenko, E. V.; Aloni, S.; Sadtler, B.; Alivisatos, A. P. Seeded Growth of Highly Luminescent Cdse/Cds Nanoheterostructures with Rod and Tetrapod Morphologies. *Nano Lett.* **2007**, *7*, 2951–2959.
31. Lita, B.; Pavol, M. J.; Dovidenko, K.; Le Tarte, L. A.; Ellis, D.; Barbuto, T.; Bansal, S.; Smentkowski, V. S.; Young, M.; Asher, S. E. *Interface Analysis in Cdte/Cds Solar Cells*; Photovoltaic Specialists Conference (PVSC), 2010 35th IEEE, 20−25 June 2010; pp 001937−001942.
32. Docampo, P.; Ball, J. M.; Darwich, M.; Eperon, G. E.; Snaith, H. J. Efficient Organometal Trihalide Perovskite Planar-Heterojunction Solar Cells on Flexible Polymer Substrates. *Nat. Commun.* **2013**, 4.
33. Small, C. E.; Chen, S.; Subbiah, J.; Amb, C. M.; Tsang, S.-W.; Lai, T.-H.; Reynolds, J. R.; So, F. High-Efficiency Inverted Dithienogermole-Thienopyrrolodione-Based Polymer Solar Cells. *Nat. Photonics* **2012**, *6*, 115–120.
34. Kim, M. S.; Yim, K. G.; Kim, S.; Nam, G.; Lee, D. Y.; Kim, J. S.; Kim, J. S.; Leem, J. Y. Growth and Characterization of

Indium-Doped Zinc Oxide Thin Films Prepared by Sol-Gel Method. *Acta Phys. Polym., A* **2012**, *121*, 217–220.
35. Kranz, L.; Schmitt, R.; Gretener, C.; Perrenoud, J.; Pianezzi, F.; Uhl, A. R.; Keller, D.; Buecheler, S.; Tiwari, A. N. *Progress Towards 14% E□cient Cdte Solar Cells in Substrate Configuration*; Photovoltaic Specialists Conference (PVSC), 2013 IEEE 39th, 16−21 June 2013; pp 1644−1648.
36. Kloper, V.; Osovsky, R.; Kolny-Olesiak, J.; Sashchiuk, A.; Lifshitz, E. The Growth of Colloidal Cadmium Telluride Nanocrystal Quantum Dots in the Presence of Cd0 Nanoparticles. *J. Phys. Chem. C* **2007**, *111*, 10336–10341.
37. Rose, D. H.; Hasoon, F. S.; Dhere, R. G.; Albin, D. S.; Ribelin, R. M.; Li, X. S.; Mahathongdy, Y.; Gessert, T. A.; Sheldon, P. Fabrication Procedures and Process Sensitivities for Cds/Cdte Solar Cells. *Prog. Photovoltaics* **1999**, *7*, 331–340.
38. Gessert, T. A.; Burst, J. M.; Wei, S. H.; Ma, J.; Kuciauskas, D.; Rance, W. L.; Barnes, T. M.; Duenow, J. N.; Reese, M. O.; Li, J. V.; Young, M. R.; Dippo, P. Pathways toward Higher Performance Cds/Cdte Devices: Te Exposure of Cdte Surface before Znte:Cu/Ti Contacting. *Thin Solid Films* **2013**, *535*, 237–240.
39. Wood, A.; Giersig, M.; Hilgendorff, M.; Vilas-Campos, A.; Liz-Marzán, L. M.; Mulvaney, P. Size Effects in ZnO: The Cluster to Quantum Dot Transition. *Aust. J. Chem.* **2003**, *56*, 1051–1057.
40. Berry, J. J.; Ginley, D. S.; Burrows, P. E. Organic Light Emitting Diodes Using a Ga:Zno Anode. *Appl. Phys. Lett.* **2008**, *92*, 193304.
41. Ohyama, M.; Kozuka, H.; Yoko, T. Sol-Gel Preparation of Transparent and Conductive Aluminum-Doped Zinc Oxide Films with Highly Preferential Crystal Orientation. *J. Am. Ceram. Soc.* **1998**, *81*, 1622–1632.
42. Gershon, T. S.; Sigdel, A. K.; Marin, A. T.; van Hest, M. F. A. M.; Ginley, D. S.; Friend, R. H.; MacManus-Driscoll, J. L.; Berry, J. J. Improved Fill Factors in Solution-Processed ZnO/Cu2O Photovoltaics. *Thin Solid Films* **2013**, *536*, 280–285.
43. Lin, H.; Irfan; Xia, W.; Wu, H. N.; Gao, Y.; Tang, C. W. Moox Back Contact for Cds/Cdte Thin Film Solar Cells: Preparation, Device Characteristics, and Stability. *Sol. Energy Mater. Sol. Cells* **2012**, *99*, 349–355.
44. Lin, H.; Xia, W.; Wu, H. N.; Tang, C. W. Cds/Cdte Solar Cells with Moox as Back Contact Buffers. *Appl. Phys. Lett.* **2010**, *97*, 123504.